





Inferring astrophysics and cosmology with individual compact binary coalescences and their gravitational-wave stochastic background

S. Ferraiuolo^{1,2,3} *, S. Mastrogiovanni² , S. Escoffier³  and E. Kajfasz³ 

¹ Università di Roma La Sapienza, 00185 Roma, Italy

² INFN, Sezione di Roma, I-00185 Roma, Italy

³ Aix Marseille Univ, CNRS/IN2P3, CPPM, Marseille, France

March 20, 2025

ABSTRACT

Gravitational waves (GWs) from compact binary coalescences (CBCs) provide a new avenue to probe the cosmic expansion, in particular the Hubble constant H_0 . The spectral sirens method is one of the most used techniques for GW cosmology. It consists of obtaining cosmological information from the GW luminosity distance, directly inferred from data, and the redshift that can be implicitly obtained from the source frame mass distribution of the CBC population. With GW detectors, populations of CBCs can be either observed as resolved individual sources or implicitly as a stochastic gravitational-wave background (SGWB) from the unresolved ones. In this manuscript, we study how resolved and unresolved sources of CBCs can be employed in the spectral siren framework to constrain cosmic expansion. The idea stems from the fact that the SGWB can constrain additional population properties of the CBCs thus potentially improving the measurement precision of the cosmic expansion parameters. We show that with a five-detector network at O5-designed sensitivity, the inclusion of the SGWB will improve our ability to exclude low values of H_0 and the dark matter energy fraction Ω_m , while also improving the determination of a possible CBC peak in redshift. Although low values of H_0 and Ω_m will be better constrained, we obtain that most on the precision on H_0 will be provided by resolved spectral sirens.

We also performed a spectral siren analysis for 59 resolved binary black hole sources detected during the third observing run with an inverse false alarm rate higher than 1 per year jointly with the SGWB. We obtain that with current sensitivities, the cosmological and population results are not impacted by the inclusion of the SGWB.

Key words. Methods: data analysis, Cosmology: cosmological parameters, Astrophysics: observations, Gravitational waves, Stochastic Background, Stars: black holes

1. Introduction

Gravitational waves (GWs) from compact binary coalescences (CBCs) offer a unique opportunity to provide new insight into the study of the expansion of the Universe, especially in light of ongoing tensions in cosmology (Di Valentino et al. (2021)). Unlike electromagnetic (EM) observables, CBCs detected through GWs carry direct information about their luminosity distance, as such they are referred to as *standard sirens* (Schutz (1986); Holz & Hughes (2005)). When combined with redshift information, we can therefore use GWs data to probe the luminosity distance-redshift relation - and hence key cosmological parameters such as the Hubble constant H_0 . However, GWs alone do not provide the source redshift. Various methods have been developed to estimate redshifts for GW events, which are essential for this purpose.

Bright sirens are a special class of standard sirens, where an EM counterpart is observed along with the GW emission. This was the case of the binary neutron star merger GW170817 detection in association with a gamma-ray burst and a subsequent kilonova (Abbott et al. (2017a)). The host galaxy for this source was identified, allowing us to obtain a precise redshift measurement and an H_0 estimate of 70^{+19}_{-8} km/s/Mpc (Abbott

et al. (2017c)). So far, GW170817 is the only event to date with an associated EM counterpart.

Most often, other detections involve *dark sirens*, such as binary black hole (BBH) mergers, with no EM counterparts. For these types of events, several methods have been proposed to obtain a statistical redshift estimation for the source. One approach involves cross-matching the event's sky localization with galaxy catalogs, assigning probabilities based on the distribution of potential host galaxies (Abbott et al. 2017b; Soares-Santos et al. 2019; Abbott et al. 2021a; Gray et al. 2020; Palmese et al. 2020; Finke et al. 2021; Gray et al. 2022; Mukherjee et al. 2024; Abbott et al. 2023d; Mastrogiovanni et al. 2023; Gray et al. 2023; Palmese et al. 2023; Bom et al. 2024). Another method, clustering-based techniques exploit correlations between gravitational-wave events and large-scale structure to constrain redshifts (Namikawa et al. 2016a; Oguri 2016; Namikawa et al. 2016b; Zhang 2018; Scelfo et al. 2020; Bera et al. 2020; Libanore et al. 2021; Mukherjee et al. 2021; Cigarrán Díaz & Mukherjee 2022; Ferri et al. 2024; Ghosh et al. 2023; Zazzera et al. 2024).

In this paper we focus on the *spectral sirens* method (Taylor et al. 2012; Farr et al. 2019; Mastrogiovanni et al. 2021; Mancarella et al. 2022; Ezquiaga & Holz 2021; Ezquiaga & Holz 2022; Mali & Essick 2024; Mancarella et al. 2024). This approach uses the inherent degeneracy between a source's red-

* sarah.ferraiuolo@univ-amu.fr

shift z and its detector frame mass m_{det} , as well as its source frame mass m_s , linked by the relation $m_{\text{det}} = (1 + z)m_s$. The sources' redshifts are indirectly inferred by measuring the detector frame masses and simultaneously modeling the source mass distribution and the cosmological parameters. The effectiveness of this method is influenced by the choice of phenomenological models used to represent the CBC source mass distribution and their ability to accurately capture the true characteristics of the CBC population (Mukherjee 2022; Gray et al. 2022; Karathanasis et al. 2023; Pierra et al. 2024; Mastrogiovanni et al. 2023a; Agarwal et al. 2024). This approach was applied to measure H_0 using 47 gravitational-wave sources from the Third LIGO and Virgo Gravitational-Wave Transient Catalog (GWTC-3) obtaining $H_0 = 68_{-7}^{+12}$ km/s/Mpc (68% credible interval) when combined with the H_0 measurement from GW170817 and its electromagnetic counterpart (Abbott et al. (2023a)).

In addition to resolved sources, we expect to detect a stochastic gravitational-wave background (SGWB) from unresolved sources. The SGWB depends on the properties of the population and the underlying population of CBCs (Romano & Cornish (2017); Christensen (1992); van Remortel et al. (2023)). The idea is to explore whether the detection or non-detection of this stochastic background, combined with the information from resolved sources, can help constrain the population properties more accurately and, in turn, refine the measurements of the cosmological parameters (Abbott et al. 2021d). Moreover, as recognized in Cousins et al. (2025), the SGWB also has a direct dependency from H_0 given by the fact that the GW energy density is related to the comoving volume. The interplay between GW signals from CBCs and the SGWB presents an exciting opportunity to improve our understanding of fundamental cosmological and astrophysical parameters.

The method of synthesizing data from individual CBC events with upper limits on the SGWB was initially examined by Callister et al. (2020), Turbang et al. (2024) in the context of astrophysical properties for CBCs and more recently by Cousins et al. (2025) for a joint cosmological and population analysis with the latest Gravitational-Wave Transient Catalog (GWTC-3). In our study, we focus more on understanding what population properties and cosmological parameters could be constrained by the SGWB for future observing runs.

This paper is organized as follows. Section 2 outlines the methodology for our integrated analysis of individual binary black hole mergers and the stochastic background. Section 3 presents how we simulate the data. We discuss our projection studies in Sec. 4 and a reanalysis with this methodology of GWTC-3 in Sec. 5. Finally in Sec. 6 we summarize our conclusions.

2. Analysis Method

We aim to infer the cosmological and population parameters including resolved and unresolved CBC. We build on the framework established by Callister et al. (2020) and Turbang et al. (2024). We describe the GW dataset as a set $\{x\}$ of N_{obs} resolved GW detections found in data chunks $\{x\} = \{x_1, \dots, x_{N_{\text{obs}}}\}$ and a set of elements $\hat{C}(f)$ describing the amount of correlated noise across GW detectors that are obtained for an observing time T_{obs} . Let Φ denote the hyperparameters that characterize the CBC population and cosmology (e.g., H_0 and Ω_m). We proceed under the assumption that the joint likelihood of these observations can be factorized as:

$$\mathcal{L}(\{x\}, \hat{C}|\Phi) = \mathcal{L}_{\text{CBC}}(\{x\}|\Phi)\mathcal{L}_{\text{SGWB}}(\hat{C}|\Phi), \quad (1)$$

where \mathcal{L}_{CBC} represents the likelihood associated with the detection of resolved sources, which, as discussed in Sec. 2.1, follows an inhomogeneous Poisson distribution. The likelihood $\mathcal{L}_{\text{SGWB}}$ denotes stochastic likelihood modelled as a Gaussian process, as detailed in Sec. 2.2. We note that the factorization of the likelihood in Eq. 6 assumes that the “stochastic” data is independent of the resolved sources. In other words, we assume that the amount of stochastic GW signal is not modified after removing all the resolved sources in the observing period T_{obs} . This might not be the case when the sensitivity of the GW detectors is enough to solve a considerable amount of the population. To address this issue while still using the same likelihood model, we propose splitting the GW data collected in an observing time T_{obs} into two disjoint sets with duration $T_{\text{obs}}/2$ and use one for detecting solved sources while the other for the SGWB.

2.1. Hierarchical Bayesian Likelihood

The detection of GWs events is modeled as an inhomogeneous Poisson process with selection biases (Mandel et al. (2019); Vitale et al. (2021)). For N_{obs} detected GWs signals over an observation time T_{obs} , the probability of obtaining a specific GWs dataset $\{x\}$ given population hyperparameters Φ is:

$$\mathcal{L}_{\text{CBC}}(\{x\}|\Phi) \propto e^{-N_{\text{exp}}(\Phi)} \prod_{i=1}^{N_{\text{obs}}} T_{\text{obs}} \int d\theta dz \times \times \mathcal{L}_{\text{GW}}(x_i|\theta, z, \Phi) \frac{1}{1+z} \frac{dN_{\text{CBC}}}{d\theta dz dt_s}(\Phi), \quad (2)$$

here, N_{exp} represents the expected number of CBC detections within the observation time T_{obs} . Typically N_{exp} is evaluated using a set of Monte Carlo injections in real data and it is used to correct for selection biases, more details are provided in the App. A. The variables z and θ denote the redshift and a set of binary parameters for each CBC, such as the source masses. The individual GW likelihood $\mathcal{L}_{\text{GW}}(x_i|\theta, z, \Phi)$ incorporates uncertainties in the parameters θ ; the final term of the equation corresponds to the CBC rate in the source frame time t_s . The model that we adopt for the CBC rate will be described in more detail in Sec. 3.

2.2. Stochastic Gravitational-Wave Background Likelihood

The SGWB is conventionally defined as (Romano & Cornish 2017):

$$\Omega_{\text{GW}}(f) = \frac{1}{\rho_c} \frac{d \ln \rho_{\text{GW}}(f)}{d \ln f}, \quad (3)$$

where $\rho_c = 3H_0^2 c^2 / (8\pi G)$ is the critical energy density of the Universe, $\rho_{\text{GW}}(f)$ is the SGWB energy density observed at the frequency f , G is Newton's gravitational constant, c is the speed of light, and H_0 is the Hubble constant. The SGWB energy density modeled from the population of CBC is given by (Phinney 2001):

$$\Omega_{\text{GW}}(f) = \frac{f}{\rho_c} \int_0^{+\infty} dz \frac{R(z)}{H(z)(1+z)} \left\langle \frac{dE_s}{df_s} \right\rangle_{f(1+z)}, \quad (4)$$

here, $R(z)$ is the event rate per unit comoving volume and per unit time at redshift z . The term $H(z)$ is the Hubble parameter that under the assumption of Λ CDM is defined as $H(z) = H_0 \sqrt{\Omega_m(1+z)^3 + \Omega_\Lambda}$ (Wei & Wu 2017). As recognized in Cousins et al. (2025), the SGWB scales as H_0^{-3} , this scaling

arises from comoving volume density term ($\propto H_0^{-3}$). The final term describes the energy spectrum radiated by the CBC population, averaged over the source population at a given redshift. More details on how we calculate the SGWB are provided in the App. A

Searches for the SGWB, such as those conducted by the LIGO-Virgo-Kagra (LVK) collaboration (Abbott et al. (2021d)), aim to measure the dimensionless energy density $\Omega_{\text{GW}}(f)$ in Eq. 4. Let us label the GW detectors in the network by the index I , the optimal cross-correlation estimator for a baseline IJ is given by Allen & Romano (1999); Abbott et al. (2021b):

$$\hat{C}_{IJ}(f) = \frac{2}{T_{\text{obs}}} \frac{10\pi^2}{3H_0^2} \frac{f^3}{\gamma_{IJ}(f)} \tilde{s}_I(f) \tilde{s}_J^*(f), \quad (5)$$

where T_{obs} is the observation time, and $\tilde{s}_I(f)$ and $\tilde{s}_J(f)$ are the Fourier transforms of the data for detectors I and J . The overlap reduction function $\gamma_{IJ}(f)$ encodes the baseline geometry of the detector pair IJ (Christensen (1992); Flanagan (1993)). The combined cross-correlation estimator using information from all baselines is obtained by:

$$\hat{C}(f) = \frac{\sum_{IJ} \hat{C}_{IJ}(f) \sigma_{IJ}^{-2}}{\sum_{IJ} \sigma_{IJ}^{-2}}, \quad (6)$$

with an expected value of $\langle \hat{C}(f) \rangle = \Omega_{\text{GW}}(f)$. We adopt the shorthand notation \sum_{IJ} meaning a sum over all independent baselines IJ . The variance of the estimator for a single baseline IJ is:

$$\sigma_{IJ}^2(f) \approx \frac{1}{2T_{\text{obs}}\Delta f} \left(\frac{10\pi^2}{3H_0^2} \right)^2 \frac{f^6}{\gamma_{IJ}^2(f)} P_I(f) P_J(f), \quad (7)$$

under the assumption of a small signal-to-noise ratio for the SGWB, where $P_I(f)$ and $P_J(f)$ are the one-sided power spectral densities of detectors I and J , and Δf is the frequency resolution. The combined variance for all pairs, assuming statistical independence, is given by:

$$\sigma^2(f) = \left(\sum_{IJ} \frac{1}{\sigma_{IJ}^2(f)} \right)^{-1}. \quad (8)$$

The variance $\sigma^2(f)$ can be used to set the upper limit on the SGWB.

The cross-correlation estimator in Eq. 6 is then used in the likelihood $\mathcal{L}_{\text{SGWB}}$, which is well-approximated by a Gaussian distribution (Abbott et al. (2021d)):

$$\mathcal{L}_{\text{SGWB}}(\hat{C}|\Phi) \propto \exp \left[-\frac{1}{2} \sum_k \left(\frac{\hat{C}(f_k) - \Omega_{\text{GW}}(f_k, \Phi)}{\sigma(f_k)} \right)^2 \right], \quad (9)$$

where the sum runs over discrete frequency bins f_k and where Ω_{GW} is our model energy-density spectrum defined in Eq. 4. We note that the stochastic likelihood is not invariant for H_0 , but it scales as H_0^{-1} . This scaling is due to the combination of the CBC energy density with the cross-correlation statistic and variance, which also matches the $1/H_0$ scaling of the SGWB SNR for detection (Cousins et al. 2025).

3. Framework to simulate GW data for O5 sensitivities

We build two observing scenarios for the simulation that are based on two years of GW data. The first one is called ‘‘Resolved CBCs’’ and it consists of 2 years of GW data that is used *only* to detect resolved sources. The second case is called ‘‘combined SGWB and CBCs’’ and it is generated with 1 year of GW data used to collect resolved sources and 1 year used to detect the SGWB. The choice of dividing the GW data into two independent sets for the resolvable sources and the SGWB is driven by the fact that we want to keep the hierarchical likelihood separable. We also have a third validation case with 1 year of GW data employed only for stochastic searches that is used to understand the actual contribution of the SGWB on the population parameters.

The common ingredient needed to simulate data for the solved GW sources and the SGWB is a population and cosmological model for the CBCs. We assume a Λ CDM cosmology (Wei & Wu 2017) and we parametrize the rate of CBCs introduced in Sec. 2 as:

$$\frac{dN_{\text{CBC}}}{d\theta dz dt_s} = R_0 \psi(z, \Phi) p_{\text{pop}}(\vec{m}_s | \Phi) \frac{dV_c}{dz} \quad (10)$$

where $R_0 = 20 \text{ Gpc}^{-3} \text{yr}^{-1}$ is the local merger rate at $z = 0$, $\psi(z, \Phi)$ is the merger rate evolution with redshift, and $p_{\text{pop}}(\vec{m}_s | \Phi)$ represents the probability density function for the source frame masses $\vec{m}_s = (m_{1,s}, m_{2,s})$. The term dV_c/dz is the differential of the comoving volume per unit redshift. For the source frame masses $m_{1,s}$ and $m_{2,s}$, we adopt a power-law plus peak (PLP) model, consistent with the LIGO and Virgo GWTC-3 results (Abbott et al. (2023c)):

$$p(m_{1,s} | m_{\min}, m_{\max}, \alpha) = (1 - \lambda_g) P(m_{1,s} | m_{\min}, m_{\max}, \alpha) + \quad (11)$$

$$+ \lambda_g G(m_{1,s} | \mu_g, \sigma_g), \quad \text{with } (0 \leq \lambda_g \leq 1)$$

$$p(m_{2,s} | m_{\min}, m_{1,s}, \beta) = P(m_{2,s} | m_{\min}, m_{1,s}, \beta), \quad (12)$$

where the primary mass $m_{1,s}$ follows a combination of a truncated power-law distribution and a Gaussian peak, weighted by the fraction λ_g . The secondary mass $m_{2,s}$ is modeled conditionally on $m_{1,s}$ using a power-law distribution. We use this model to describe a population of BBHs. The PLP model is motivated by the fact there is a potential accumulation of CBC around $35M_\odot$ just before the pair-instability supernovae gap (Talbot & Thrane 2018). In both distributions, we applied a smoothing window at the low end of the mass distribution dependent on a parameter δ_m representing the smoothing length. This is introduced to model the effects of the stellar progenitor metallicity (Abbott et al. 2021c). The redshift evolution $\psi(z, \Phi)$, is modeled using a rate model Madau & Dickinson (2014); Callister et al. (2020), which is expressed as:

$$\psi(z, \Phi) = \left[1 + (1 + z_p)^{-\gamma-\kappa} \right] \frac{(1+z)^\gamma}{\left(1 + \frac{1+z}{1+z_p} \right)^{\gamma+\kappa}}, \quad (13)$$

where γ governs growth at low redshift, z_p marks the transition redshift, and κ determines the decline at high redshift. The hyperparameters’ values assumed for the population are reported in Tab. 1. According to the rate model, the total number of BBH coalescences in one year in all of the universe is about 10^6 , which agrees with existing literature (Borhanian & Sathyaprakash 2024; Ng et al. 2021).

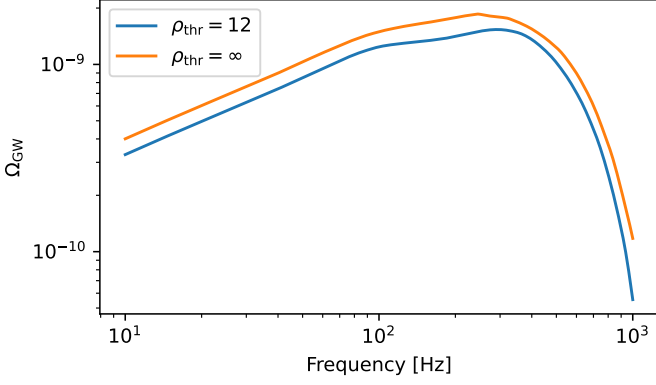


Fig. 1. Stochastic gravitational-wave background calculated for the population of BBH sources (orange line) and after removing all the BBHs with SNR > 12 (blue line). The average SGWB power loss is about 30% in all the sensitivity bands for ground-based GW detectors.

3.1. Resolved Gravitational Wave Sources

To simulate resolved GW sources, we generate a population of BBHs following the previously described population model. We use a simulative approach similar to Fishbach et al. (2020) and make simplified assumptions to calculate the BBHs signal-to-noise ratio (SNR) and the uncertainties for the measure of the binary parameters. For each binary, we compute the detector chirp mass M_{chirp} , symmetric mass ratio η , and luminosity distance d_L . The optimal SNR ρ_{true} of the binary is calculated with the approximation used in Fishbach et al. (2020); Mastroianni et al. (2021):

$$\rho_{\text{true}} = \rho_0 \theta \left(\frac{M_{\text{chirp}}}{M_{\text{chirp},0}} \right)^{5/6} \frac{d_{L,0}}{d_L}, \quad (14)$$

where $\rho_0 = 12$ is the reference SNR for a binary system with a chirp mass of $M_{\text{chirp},0} = 26 M_\odot$ and a luminosity distance $d_{L,0} = 1.9$ Gpc, consistent with the expected sensitivities for the O5 observing run (Abbott et al. 2020). The projection factor θ accounts for the binary’s orientation relative to the detector network, we defined it as the quadratic sum of the combined antenna response functions F_+ and F_\times (Yunes & Siemens 2013).

To include the effects of noise across multiple detectors, we simulate an observed SNR, ρ_{det} , by accounting for noise realizations in each detector. Specifically, we sample ρ_{det} using a non-central χ^2 distribution with a non-centrality parameter ρ_{true}^2 and $2 \times N_{\text{detectors}} = 10$ degrees of freedom. In this simulation, we apply a detection threshold of $\rho_{\text{det}} > 12$.

With the previous choices, we obtained that the resolvable sources correspond to about 0.6% of the overall BBH population. In Fig. 1, we show the SGWB before and after removing the resolvable sources. As we can observe, for this simulative scenario, removing the resolvable individual sources would decrease the SGWB by $\sim 30\%$. As a consequence, the likelihood in Eq. 1 is not separable and that is the motivation for which our “Combined SGWB and CBCs” scenario splits two years of GW data into two independent datasets for the resolved sources and the SGWB sources. The set “Resolved CBCs” contains about 1200 events detected, while the set “Combined SGWB and CBCs” contains about 600 solved events.

Once detections are identified, posterior samples are generated using a likelihood model described as follows:

$$\begin{aligned} \mathcal{L}(\rho_{\text{det}}, \log(M_{\text{chirp, det}}), \theta_{\text{det}}, \eta_{\text{det}} | \rho, \log(M_{\text{chirp}}), \theta, \eta) = \\ = \mathcal{L}(\rho_{\text{det}} | \rho) \mathcal{L}(\log(M_{\text{chirp, det}}) | \log(M_{\text{chirp}})) \mathcal{L}(\theta_{\text{det}} | \theta) \mathcal{L}(\eta_{\text{det}} | \eta), \end{aligned} \quad (15)$$

where $\mathcal{L}(\rho_{\text{det}} | \rho)$ as we said follows a non-central χ^2 distribution, while other for M_{chirp} , η , and θ we used the following normal distribution for the likelihoods:

$$\mathcal{L}(\log(M_{\text{chirp, det}}) | \log(M_{\text{chirp}})) = \mathcal{N}\left(\log(M_{\text{chirp}}), 0.08 \frac{8}{\rho_{\text{det}}}\right), \quad (16)$$

$$\mathcal{L}(\theta_{\text{det}} | \theta) = \mathcal{N}\left(\theta, 0.21 \frac{8}{\rho_{\text{det}}}\right), \quad (17)$$

$$\mathcal{L}(\eta_{\text{det}} | \eta) = \mathcal{N}\left(\eta, 0.02 \frac{8}{\rho_{\text{det}}}\right). \quad (18)$$

After obtaining posterior samples distributed according to this likelihood model with uniform priors, we converted them into source frame masses and luminosity distance using the SNR conversion Eq. 14. Since there is an implied prior in this transformation, it is removed by calculating the Jacobian of the transformation from $(\rho_{\text{det}}, M_{\text{chirp, det}}, \eta_{\text{det}}, \theta_{\text{det}})$ to the final variables required for our analysis $(m_{1,s}, m_{2,s}, d_L)$.

An example of the posterior distributions for key parameters, including detector frame masses and luminosity distance, is shown in Fig. 2. With this type of likelihood, we can see that it reproduces correlated mass estimates, as expected for real GW events.

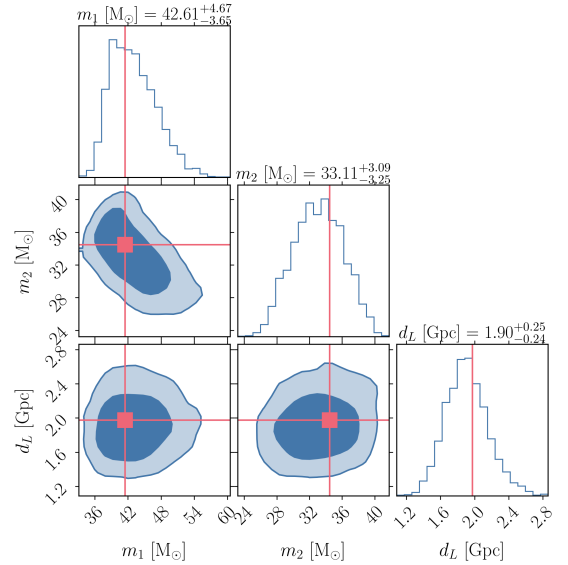


Fig. 2. Corner plot showing the posterior distributions of the key parameters estimated from the simulation (blue). The red lines represent the true values of the parameters injected into the simulation. The diagonal panels display the marginalized 1D posterior distributions for each parameter, while the off-diagonal panels show the 2D joint posterior distributions.

3.2. Stochastic Gravitational Wave Background

We simulate cross-correlation measurements of the corresponding SGWB, assuming $T_{\text{obs}} = 1$ yr of integration with LVK with O5 sensitivity and a coherence time for the stochastic search of

4 seconds. This corresponds to frequency point estimates of the cross-correlation statistic evaluated every 0.25 Hz. As a detector baseline we use a five-detector LIGO (Hanford, Livingston and India), Virgo and KAGRA networks at design sensitivities¹ (Acernese 2014; Aasi 2015; Aso et al. 2013; UNNIKIRISHNAN 2013).

In Fig. 3, each data point is drawn from a Gaussian distribution centered on the true value of $\Omega_{\text{GW}}(f)$, as calculated using Eq. 4, with a standard deviation $\sigma(f)$ given by Eq. 8. The uncertainty $\sigma(f)$ represents the sensitivity to an SGWB in every frequency bin. As argued before, $\sigma(f)$ is directly related to the upper limits of the energy density of the SGWB, as fluctuation beyond this value is rare. This property allows us to detect the SGWB: if $\sigma(f)$ is much larger than $\Omega_{\text{GW}}(f)$, the variations in $\Omega_{\text{GW}}(f)$ become effectively indistinguishable within the noise, making detection unlikely. Conversely, when $\sigma(f)$ is sufficiently small, deviations in $\Omega_{\text{GW}}(f)$ can be resolved, enabling us to identify the SGWB signal. Figure 3 also shows why low H_0 values

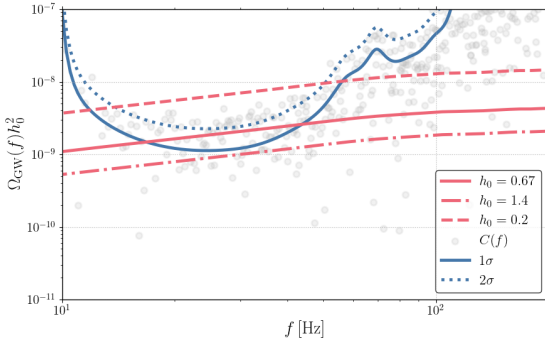


Fig. 3. Simulated SGWB cross-correlation spectrum $C(f)$ (points) with corresponding uncertainties $\sigma(f)$ (grey lines). The red lines are theoretical curves of $\Omega_{\text{GW}}(f)$ for different h_0^2 , and the blue curves display the 1σ and 2σ sensitivity of the LVK at the design sensitivity (1 year of observation in O5). The scatter reflects realistic fluctuations centered on the true $\Omega_{\text{GW}}(f)$.

are easier to exclude with the SGWB. As we can observe, when we remove the $1/H_0^2$ dependency, namely when we normalize the critical density of the Universe ρ_c , the cross-correlation coefficients do not depend on H_0 (as also indicated in Eq. 5), while the SGWB does. As a result, the SNR for the SGWB increases as $1/H_0$.

4. Results with simulated data

Using the simulated data described in Sec. 3 and prior ranges adopted are listed in Tab. 1. We perform three separate analyses. The first considers only resolved CBC events (“Resolved CBCs”), using two years of data. The second is a combined analysis (“Combined SGWB and CBCs”), where we use one year of resolved BBH detections and one year of SGWB measurements. Finally, the third analysis focuses solely on one year of the SGWB to assess its sensitivity and, if possible, directly observe the impact of improvements due to unresolved sources.

Figure 4 displays the corner plot for the cosmological parameters H_0 and Ω_m with the redshift rate parameters. From the analysis using only resolved CBCs, we find $H_0 = 59.7^{+17.1}_{-13.4}$ km s⁻¹Mpc⁻¹ at 68% credible interval (CI). Combining SGWB information we find $H_0 = 66.2^{+19.3}_{-12.1}$ km s⁻¹Mpc⁻¹ at

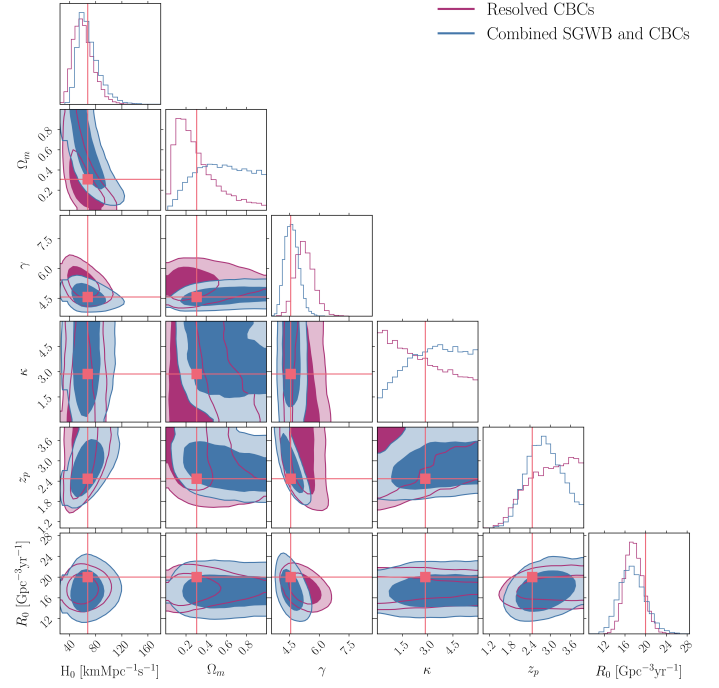


Fig. 4. Posterior on the population parameters governing the cosmic expansion and the CBC merger rate as a function of redshift for the data set “Resolved CBCs” (2yrs) of observations and the data set “Combined SGWB and CBCs” (1 yr for individual sources and 1 yr for the SGWB). The injected values are marked with the orange dot.

68% CI, indicating no significant improvement in precision. This result indicates that most of the precision on H_0 is determined by resolved spectral sirens. However, we note that the inclusion of the SGWB significantly helps in excluding the region of the parameter space that covers low values of H_0 and Ω_m . As also indicated by Cousins et al. (2025), this is a consequence of the fact that the SNR for the SGWB detection is higher for low values of H_0 and Ω_m .

We observe that both the data sets for individual sources and SGWB measure the rate parameter R_0 with similar precision. This is a consequence of the fact that the individual sources are mostly detected at lower redshifts and are the ones driving the inference on these population parameters. On γ we achieve an additional 10% precision with the combined analysis. We also see that the inclusion of the SGWB slightly introduces some preferences for the posteriors on z_p and k . These two parameters govern the peak of the BBH merger rate and its redshift evolution for $z > z_p$. The inclusion of the stochastic background makes possible the measurement $z_p = 2.8^{+0.6}_{-0.5}$ and helps to exclude low values of k , namely, we exclude models in which the rate increases beyond z_p .

Figure 5 focuses on the mass model parameters and correlations with H_0 . The combined analysis does not lead to any improvement in these parameters, whereas the resolved-only analysis performs better.

To assess the performance of the inference, we produce posterior predictive checks (PPCs), which are defined as:

$$p(\theta|x) = \int p(\Phi|x)p(\theta|\Phi)d\Phi, \quad (19)$$

$$\Omega_{\text{GW}}(f|x) = \int p(\Phi|x)\Omega_{\text{GW}}(f;\Phi)d\Phi, \quad (20)$$

¹ <https://dcc.ligo.org/LIGO-T2000012-v1/public>

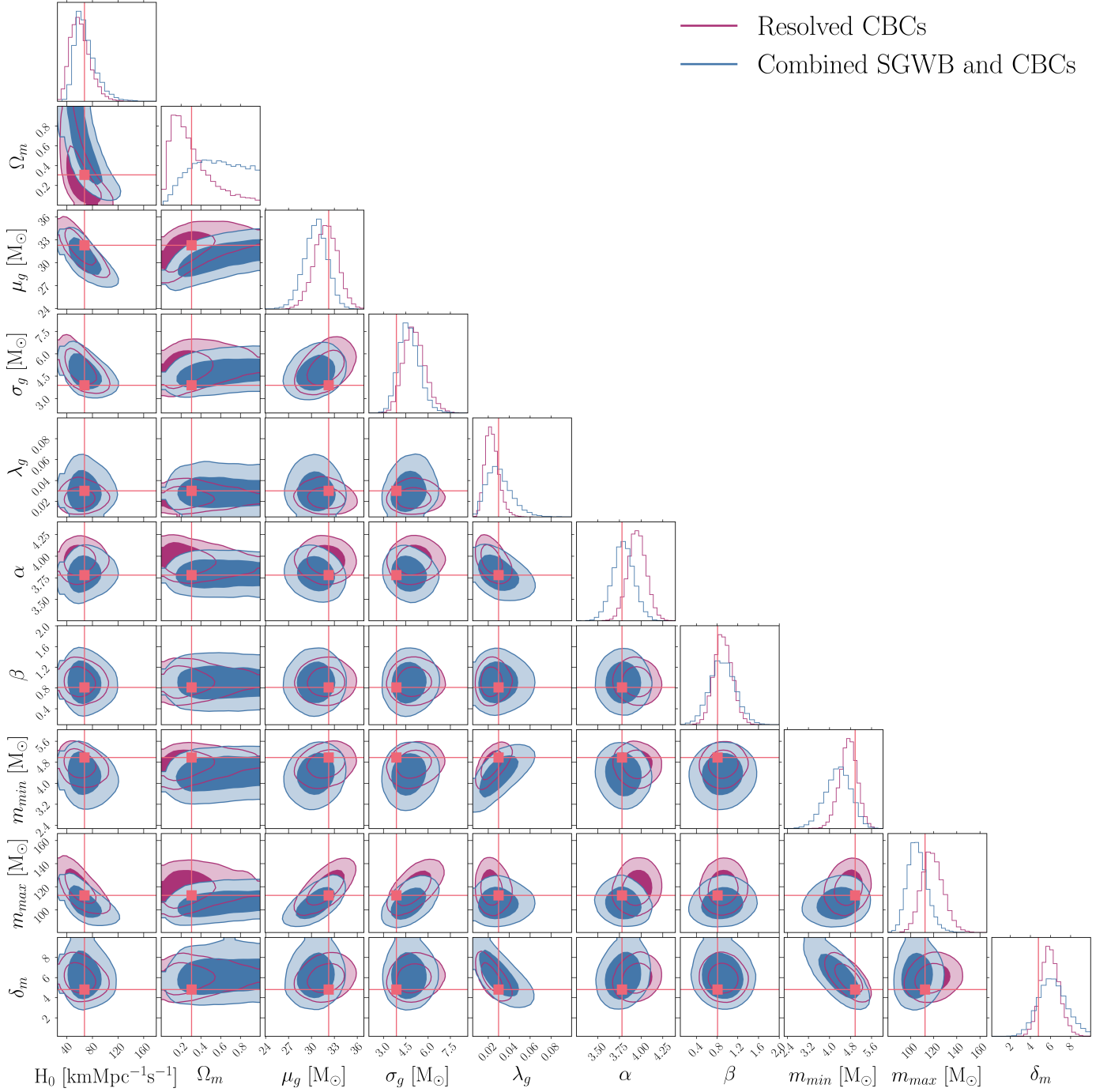


Fig. 5. Posterior on the population parameters governing the cosmic expansion and the CBC mass parameters for the data set “Resolved CBCs” (2 yrs) of observations and the data set “Combined SGWB and CBCs” (1 yr for individual sources and 1 yr for the SGWB). The injected values are marked with the orange dot.

where $p(\Phi|x)$ represents the posteriors on the population parameters and $\{x\}$ the GW data that can either include or not the SGWB. By analyzing the PPCs for all three analyses in Fig. 6 we gain insight into the reconstructed redshift distribution (top panel), mass distribution (middle panel), and SGWB energy density (bottom panel), $\Omega_{GW}(f)$. In Fig. 6 we report the posterior predictive checks for the analyses that we have performed. When considering resolved sources alone, the reconstructed redshift distribution is precise at low redshifts, while at higher redshifts $z \geq z_p$, the PPC is highly prior-dominated as we can not determine the values of k and z_p . When using the SGWB-only data,

the reconstruction of the rate is strongly prior-dominated as there is too much degeneracy among the rate parameters R_0 , γ and k , although there appears to be some information on the values of z_p . Including individual sources and SGWB together, provides a reconstruction of the rate informative up to redshift $z = 2 - 3$ consistent with what is observed in (Callister et al. 2020). As we can see, by combining the resolved sources and the SGWB, the reconstruction of the BBH merger rate is less prior-dominated.

For the mass spectrum, we obtain that most of the information is collected from individual sources. In fact, for the SGWB-only analysis, the reconstruction of the mass spectrum is strongly

prior dominated. The improvement in the precision of the reconstruction of SGWB energy density, when considering individual and SGWB sources, is mostly due to the improvement in the measure of γ and z_p implied by the CBC rate parameters.

5. Reanalysis of GWTC-3

Using the approach defined in Sec. 2 and the likelihood in Eq. 1, we reperform a population and cosmological spectral siren run with data from the latest public LVK observing run.

We select 59 BBHs detected during O3 with an inverse false alarm rate higher than 1 yr and we use their posteriors released with GWTC-3 (Abbott et al. 2023b). To correct selection biases for the Poisson part of the likelihood, we use a set of injections in real O3 data² released with Abbott et al. (2023c). For the stochastic data, we use the frequency point estimation of $\hat{C}(f)$ and $\sigma^2(f)$ released³ with Abbott et al. (2021b). We only consider frequencies below 200 Hz to ease the computational load of the analysis. The $\hat{C}(f)$ that we use are evaluated every 0.03 Hz, corresponding to a coherence time for the SGWB search of 32 s and they are calculated with $H_0 = 67.9 \text{ km s}^{-1} \text{ Mpc}^{-1}$. For this analysis, we still use the same BBH merger redshift model considered for the simulations. While for the mass model, we adopt a **MULTI PEAK** model, that can describe also a possible feature at masses $\sim 10M_\odot$. The **MULTI PEAK** model describes the mass distributions as

$$p(m_{1,s}|m_{\min}, m_{\max}, \alpha) = (1 - \lambda_g)P(m_{1,s}|m_{\min}, m_{\max}, \alpha) + \lambda_g \lambda_{g,\text{low}} G(m_{1,s}|\mu_{g,\text{low}}, \sigma_{g,\text{low}}) + \lambda_g (1 - \lambda_{g,\text{low}}) G(m_{1,s}|\mu_{g,\text{high}}, \sigma_{g,\text{high}}), \quad (21)$$

$$p(m_{2,s}|m_{\min}, m_{1,s}, \beta) = P(m_{2,s}|m_{\min}, m_{1,s}, \beta). \quad (22)$$

For the reanalysis of O3, we also make the implicit assumption that the likelihood in Eq. 1 is separable. For the O3 runs, this is a reasonable assumption as the removal of the individual sources of the population does not modify significantly the SGWB (Abbott et al. 2021b). The priors used for the analysis are reported in Tab. 1.

We perform two analyses, one considering only individual sources and the other considering also the SGWB upper limits. We find that the constraints on the population parameters, including also the cosmological parameters, are entirely given by the individual GW sources. In Fig. 7, we display the marginalized joint posterior distributions for these two analyses on the Hubble constant, Ω_m and the parameter γ for the rate evolution. We find that the inclusion of the SGWB weakly helps in excluding low values of H_0 and high values of γ from the 2σ CI areas. The posterior on the remaining of the population parameters is unchanged and we do not display it. In Fig. 8, we show the PPCs for the BBHs rate, mass distribution and SGWB reconstructed from the two analyses. We notice that the mass and rate reconstructions are equivalent in the case that the SGWB is included or not. We can also see that the reconstructed SGWB in both analyses is well below the 1σ upper limits from the stochastic searches. This means that the SGWB prediction is entirely given by the individual sources of CBCs and no additional information can be included from the SGWB likelihood. This is consistent with what was found in Callister et al. (2020).

In parallel to this work, Cousins et al. (2025) presented a spectral siren analysis using GWTC-3 including also the SGWB. Although the results that we obtained are in excellent agreement,

namely the inclusion of the SGWB does not modify significantly the inference on population and cosmological parameters, there are few technical differences in our approach. From a data selection point of view, Cousins et al. (2025) uses 42 BBH events with $\text{SNR} > 11$ observed in the first three LIGO and Virgo observing while we consider 59 BBHs detected during O3 with inverse false alarm rate higher than 1 per year. Another difference is that Cousins et al. (2025) uses a **Power Law + peak** model to describe the masses while we use a **Multi Peak** model. From a data analysis perspective, Cousins et al. (2025) uses as a prior on the population and cosmological parameters the posterior in Abbott et al. (2023a) from the spectral siren analysis. This is motivated indeed by the separability of the likelihood in Eq. 1 that we also assume in our framework. Then the SGWB information is included as a likelihood term fitting posterior samples from Abbott et al. (2021b) on $\Omega_{\alpha=2/3}$, which is a quantity describing a SGWB as

$$\Omega_{\text{GW}}(f) = \Omega_{\alpha=2/3} \left(\frac{f}{f_{\text{ref}}} \right)^{2/3}, \quad (23)$$

and corresponds to the SGWB expected by a population of BBHs emitting GWs during their inspiral phase at the 0 Post-Newtonian order. Instead, we calculate Ω_{GW} reweighting a GW energy spectrum that is calculated considering corrections for the GW emission up to the 3.5 Post-Newtonian order (Ajith et al. 2008) and also for the merger and ring-down phases. However, we notice that our two approaches reach equivalent results as the SGWB is dominated in the 20 – 200 Hz region by the inspiral of BBH merger that can be safely estimated with the 0 Post-Newtonian order emission, therefore in that region, the SGWB is well approximated by the prescription in Eq. 23.

6. Conclusions

In this work, we discussed how it is possible to include the SGWB into spectral siren analyses for GW cosmology and enhance our understanding of astrophysical populations and cosmological parameters. Using simulated data at design sensitivity of the LVK network's O5 observing run, we applied a hierarchical Bayesian framework to infer a set of 14 hyperparameters Φ , constraining key cosmological parameters such as H_0 and Ω_m , along with parameters governing the CBC mass distribution and the redshift evolution of the merger rate.

Our analysis shows that combining SGWB data into the inference framework does not improve the precision on the marginal posteriors for cosmological parameters. In particular, we see that the Hubble constant estimates derived solely from resolved events yielded $H_0 = 59.7^{+17.1}_{-13.4} \text{ km s}^{-1} \text{ Mpc}^{-1}$ at 68% CI, while combining the SGWB information yielded $H_0 = 66.2^{+19.3}_{-12.1} \text{ km s}^{-1} \text{ Mpc}^{-1}$ at 68% CI, indicating no significant improvement in precision. However, we obtain that the inclusion of the SGWB helps in excluding the lowest values of H_0 and Ω_m . Besides cosmology, on an astrophysical population-level, the integration of SGWB data slightly improves our understanding of the redshift evolution of CBC rates, it helps the measurements of γ and z_p . The SGWB's sensitivity to unresolved sources at higher redshifts allows for tighter constraints at high redshifts of the merger rate distribution.

When analyzing real O3 data, we find that the inclusion of the SGWB does not significantly improve any of the population or cosmological parameters. This result is consistent with the same findings of Callister et al. (2020); Abbott et al. (2021c) for population studies and Cousins et al. (2025) for the cosmological expansion parameters, and it is a consequence of the fact

² <https://zenodo.org/records/5636816>

³ <https://dcc.ligo.org/LIGO-G2001287/public>

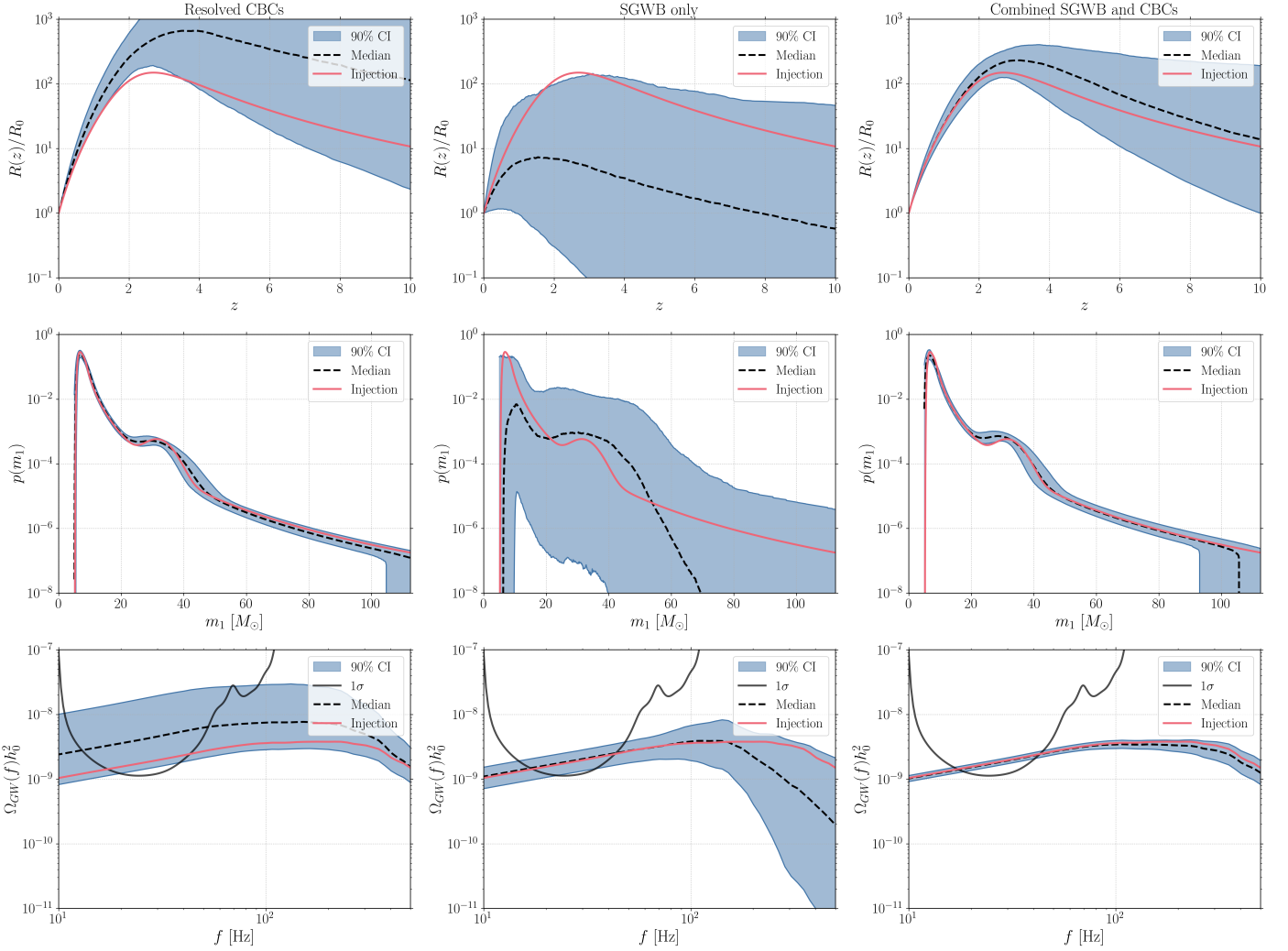


Fig. 6. Posterior predictive checks are shown for resolved CBC (left), SGWB-only analysis (center), and the joint analysis of both sources (right). The dashed and solid black curves show the median and 90% credible bounds and the red curve is the fiducial value injected. The top panel shows the rate density $R(z)$ of binary black hole mergers over the local merger rate R_0 as a function of redshift. The middle panel shows the primary mass distribution as a function of the primary mass. The bottom panel shows the posterior on $\Omega_{\text{GW}} h_0^2$ as a function of the frequency. In these panels, the black line represents the 1σ curve.

that the SGWB implied by individual sources is well below the sensitivity estimates for current stochastic searches.

Of course, in this exploratory study, we made a few simplistic assumptions that can be revised for follow-up studies. First, to preserve the separability of the likelihood in Eq. 1, we made the suboptimal choice of splitting the data disjoint sets used either for the SGWB or individual sources searches. This assumption can be improved by developing a likelihood that takes into account additional correlations on the detected sources. In this sense, we expect our results for the improvement on the determination of the cosmological parameters to be “conservative”, as we are not using the full information present in the data set. We expect that, with a joint likelihood for resolved sources and SGWB, the precision on the cosmological parameters could be improved when including the stochastic. We also did not consider the possible contribution for the SGWB introduced by binary neutron stars and neutron star black holes binaries, that can be modeled with multi-population models.

Acknowledgements. We are grateful to M. Mancarella, A. Renzini and A. Toubiana for discussions during the development of this work. We are grateful to Cousins et al. (2025) and collaborators for the constructive feedback received during the internal LVK review of this work. This work received support from

the French government under the France 2030 investment plan, as part of the Excellence Initiative of Aix Marseille University - amideX (AMX-19-IET-008 - IPhU). SM is supported by ERC Starting Grant No. 101163912–GravitySirens. This research made use of data, software and/or web tools obtained from the Gravitational Wave Open Science Center, a service of the LIGO Scientific Collaboration, the KAGRA Collaboration and the Virgo Collaboration. This material is based upon work supported by NSF’s LIGO Laboratory which is a major facility fully funded by the National Science Foundation. The authors are grateful for computational resources provided by the LIGO Laboratory (LHO) and supported by National Science Foundation Grants PHY-0757058 and PHY-0823459.

Table 1. Overview of population hyperparameters and prior choices. $U(\cdot)$ represents a uniform distribution. The POWER LAW + PEAK model is used only for the simulations in Sec. 4, while the MULTI + PEAK model is used for the analysis of O3 data in Sec. 5. The priors used on cosmological parameters and rate evolution parameters are the same for the simulation and real data cases. For the simulation case, we also report the injected value. The rate parameters, mass model parameters and H_0 are chosen to be consistent with the posterior distributions from (Abbott et al. 2023a) while Ω_m is set by (Ade et al. 2016).

Parameter	Definition	Injected Value	Prior Range
Cosmological Parameters (flat ΛCDM)			
H_0	Hubble parameter [$\text{km s}^{-1} \text{Mpc}^{-1}$]	67.7	$U(10, 200)$
Ω_m	Matter density parameter	0.3065	$U(0, 10)$
Rate Evolution (Madau-rate)			
γ	Evolution slope for $z < z_p$	4.56	$U(0, 12)$
κ	Evolution slope for $z > z_p$	2.86	$U(0, 6)$
z_p	Redshift of peak rate	2.47	$U(0, 4)$
R_0	Local merger rate [$\text{Gpc}^{-3} \text{yr}^{-1}$]	20	$U(0, 100)$
Mass Function Parameters (PowerLaw+Peak)			
α	Power-law index of primary mass	3.78	$U(1.5, 12)$
β	Power-law index of secondary mass	0.81	$U(-4, 12)$
δ_m	Smoothing parameter [M_\odot]	4.8	$U(0, 10)$
m_{\min}	Minimum source mass [M_\odot]	4.98	$U(2, 10)$
m_{\max}	Maximum source mass [M_\odot]	112.5	$U(50, 200)$
μ_g	Mean of the Gaussian peak [M_\odot]	32.27	$U(20, 50)$
σ_g	Width of the Gaussian peak [M_\odot]	3.88	$U(0.4, 10)$
λ_g	Fraction of events in the Gaussian peak	0.03	$U(0, 1)$
Mass Function Parameters (Multi + peak)			
α	Power-law index of primary mass		$U(1.5, 12)$
β	Power-law index of secondary mass		$U(-4, 12)$
m_{\min}	Minimum source mass [M_\odot]		$U(2, 10)$
m_{\max}	Maximum source mass [M_\odot]		$U(50, 200)$
δ_m	Smoothing parameter [M_\odot]		$U(0, 10)$
$\mu_{g,\text{low}}$	Mean of the lower Gaussian peak [M_\odot]		$U(7, 12)$
$\mu_{g,\text{high}}$	Mean of the higher Gaussian peak [M_\odot]		$U(20, 50)$
$\sigma_{g,\text{low}}$	Width of the lower Gaussian peak [M_\odot]		$U(0.4, 5)$
$\sigma_{g,\text{high}}$	Width of the higher Gaussian peak [M_\odot]		$U(0.4, 10)$
λ_g	Fraction of events in the peaks		$U(0, 1)$
$\lambda_{g,\text{low}}$	Fraction of events in the lower peak		$U(0, 1)$

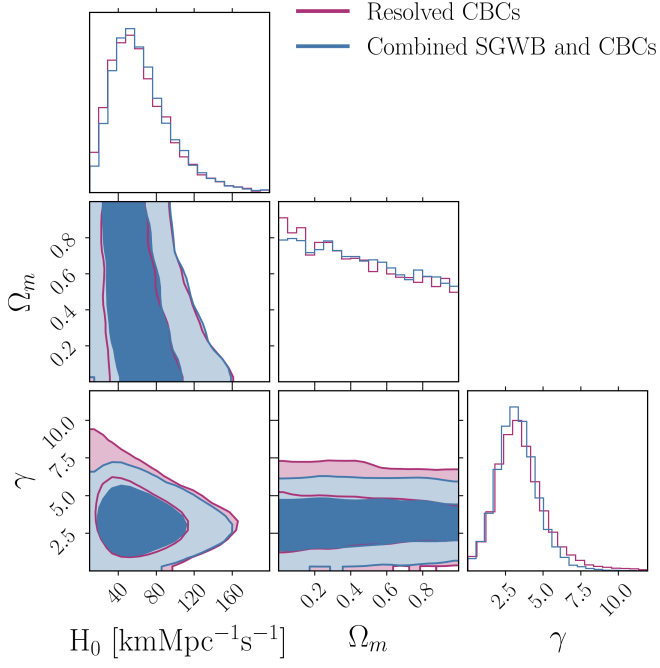


Fig. 7. Marginalized joint posterior distribution on the cosmological expansion parameters, and the rate parameter γ for an analysis including only 59 BBHs detected in O3 (purple line) and considering also the SGWB (blue line). The contour marks the 1 σ and 2 σ CIs.

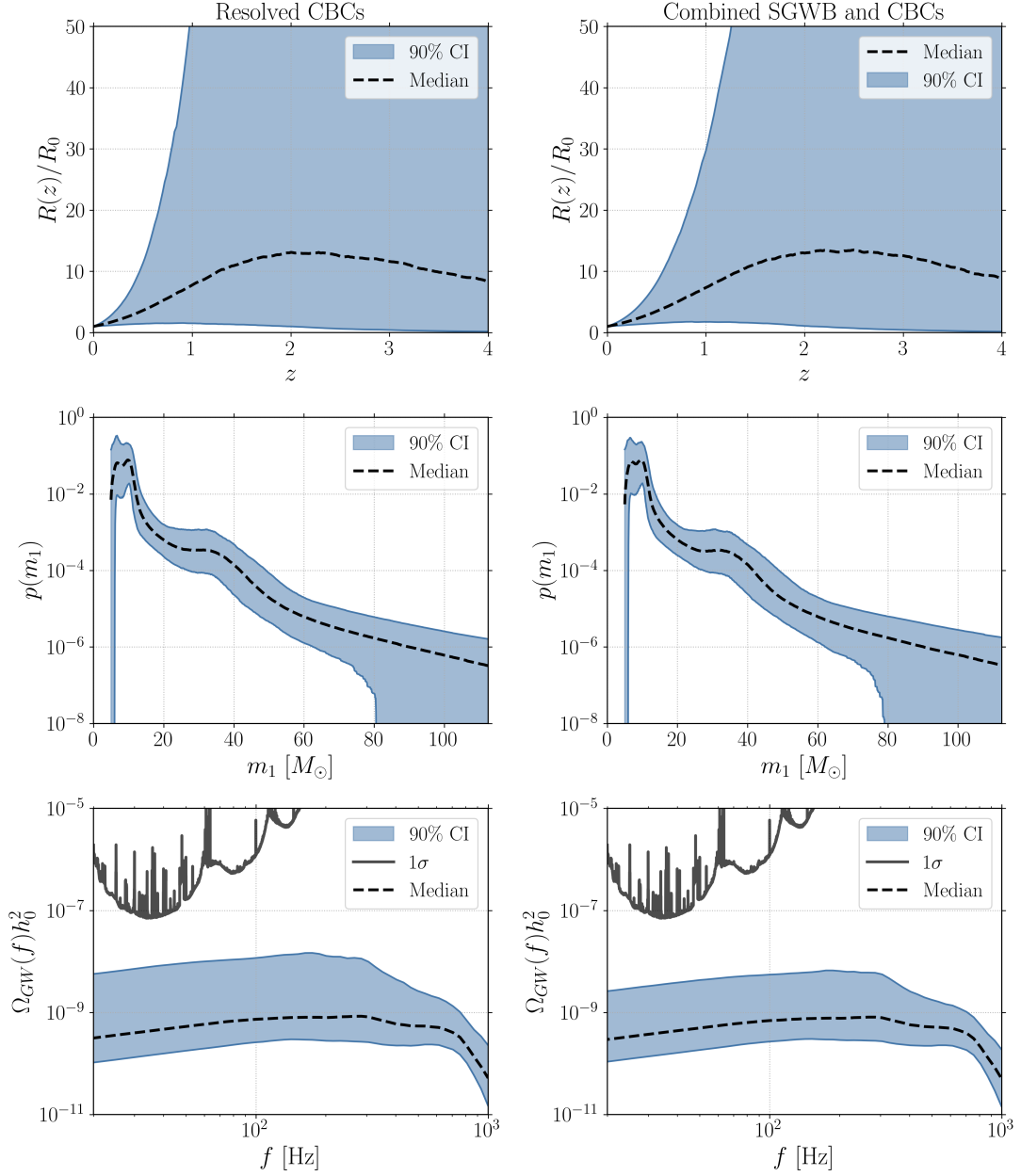


Fig. 8. Posterior predictive checks are shown for resolved CBC (left), and the joint analysis of both sources (right). The dashed and solid black curves show the median and 90% credible bounds and the red curve is the fiducial value injected. The top panel shows the rate density $R(z)$ of binary black hole mergers over the local merger rate R_0 as a function of redshift. The middle panel shows the primary mass distribution as a function of the primary mass. The bottom panel shows the posterior on $\Omega_{\text{GW}}h_0^2$ as a function of the frequency. In these panels, the black line represents the 1σ curve.

Appendix A: Computation of Hierarchical and Stochastic Likelihoods

We use the Python package `ICAROGW` to analyze our data. For a detailed explanation of its functionality, refer to Mastrogiovanni et al. (2023b). Here, we provide a summary of the likelihood computation. The main application of `ICAROGW` is to infer the population parameters Φ that describe the production rate of events in terms of the GW parameters θ , namely $\frac{dN}{d\theta}(\Phi)$. The hierarchical likelihood in Eq. 2, introduced in Section 2.1, models the probability of observing N_{obs} observations, each described by some parameters θ , in a dataset $\{x\}$ over an observing time T_{obs} accounting for selection biases (Vitale et al. 2021). `ICAROGW` computes numerically the hierarchical likelihood in Eq. 2 as:

$$\ln[\mathcal{L}(\{x\}|\Phi)] \approx -\frac{T_{\text{obs}}}{N_{\text{gen}}} \sum_{j=1}^{N_{\text{det}}} s_j + \sum_{i=1}^{N_{\text{obs}}} \ln \left[\frac{T_{\text{obs}}}{N_{s,i}} \sum_{j=1}^{N_{s,i}} w_{i,j} \right], \quad (\text{A.1})$$

where $w_{i,j}$ and s_j are weights: $w_{i,j}$ has a dimension equal to the number of CBC mergers happening per unit of time and weights the sample, while s_j weights the injections and it is defined with the dimension of a CBC merger rate per detector time. The first term derives from Monte Carlo integration to estimate:

$$N_{\text{exp}}(\Phi) = T_{\text{obs}} \int p_{\text{det}}(\theta, \Phi) \frac{dN}{d\theta} d\theta, \quad (\text{A.2})$$

where $p_{\text{det}}(\theta, \Phi)$ is a detection probability or selection bias. Since an analytical form of $p_{\text{det}}(\theta, \Phi)$ is typically unavailable, selection biases are evaluated using Monte Carlo simulations of injected and detected events (Abbott et al. 2021c). `ICAROGW` takes in input a set of N_{det} detected injections out of N_{gen} total injections generated from a prior $\pi_{\text{inj}}(\theta)$ to calculate the selection bias.

For each population model, `ICAROGW` calculates two numerical stability estimators. The first is the effective number of posterior samples per event:

$$N_{\text{eff},i} = \frac{\left(\sum_{j=1}^{N_{s,i}} w_{i,j} \right)^2}{\sum_{j=1}^{N_{s,i}} w_{i,j}^2}, \quad (\text{A.3})$$

which ensures sufficient samples contribute to the integral, with a typical threshold of at least 20 effective samples per event. The second is the effective number of injections:

$$N_{\text{eff},\text{inj}} = \frac{\left[\sum_{j=1}^{N_{\text{det}}} s_j \right]^2}{\left[\sum_{j=1}^{N_{\text{det}}} s_j^2 - N_{\text{gen}}^{-1} \left(\left[\sum_{j=1}^{N_{\text{det}}} s_j \right]^2 \right) \right]}, \quad (\text{A.4})$$

where numerical stability typically requires $N_{\text{eff},\text{inj}} > 4N_{\text{obs}}$.

The likelihood computation involves technical flags for configuration: `nparallel=2048`, which is the number of posterior samples that will be used per event to compute $w_{i,j}$, `neffPE` = -1, which is the effective number of posterior samples PE per event in Eq. A.3 and `neffINJ=None`, which is the effective number of injections required by the hierarchical likelihood. If `neffINJ=None`, a default threshold of `NeffINJ=4 × Nobs` will be used.

We developed and implemented in `ICAROGW` a new function to calculate the SGWB likelihood, as described in Eq. 9, optimizing the computation of Ω_{GW} . The expected $\Omega_{\text{GW}}(f)$ calculation, conditioned on a set of hyperparameters Φ , follows the form outlined in Eq. 4. This value depends on the average energy $\left\langle \frac{dE}{df_s} \right\rangle$ radiated by individual binaries, which is expressed as:

$$\left\langle \frac{dE}{df_s} \right\rangle = \int d\Phi p(\Phi) \frac{dE_s}{df_s}(\Phi), \quad (\text{A.5})$$

where Φ denotes the intrinsic properties of a given binary (masses, redshift, etc.), $p(\Phi)$ is the distribution of these parameters across the CBC population and this quantity is evaluated at the source-frame frequency $f_s = f(1+z)$ in Eq. 4. The GW energy spectrum is calculated with functionalities from `PyGWB` Renzini et al. (2023) and Turbang et al. (2024) that calculated the GW energy spectrum up to the 3.5 Post-Newtonian order for the GW emission and the merger and ring-down phase for non-precessing binaries.

Here, the integration spans the component masses m_1 and m_2 . Extending this to include integration over redshift, the computation of the expected $\Omega_{\text{GW}}(f)$ becomes a three-dimensional integral. A practical alternative is to use Monte Carlo integration following the methodology used in Turbang et al. (2024), which estimates the integral by averaging over numerous samples drawn from the population.

In the implementation of this approach, we start by generating N random samples from uniform distributions for the parameters z , m_1 , and m_2 . Let the i -th sampled set of parameters be denoted as $\{z_i, m_{1,i}, m_{2,i}\}$. For each of these samples, we calculate the energy spectrum denoted as $\left(\frac{dE}{df_s} \right)_i$. However, to evaluate $\Omega_{\text{GW}}(f)$ for the population described by the hyperparameters Φ , reweighting of these samples is necessary. The computation is expressed schematically as:

$$\Omega_{\text{GW}}(f) \propto \frac{1}{N} \sum_{i=1}^N w_i \left(\frac{dE}{df_s} \right)_i, \quad (\text{A.6})$$

where w_i are weights defined as:

$$w_i \propto \frac{\mathcal{R}(z_i)(1+z_i)H(z_i)^{-1}p(m_{1,i})p(m_{2,i})}{p_{\text{draw}}(z_i)p_{\text{draw}}(m_{1,i})p_{\text{draw}}(m_{2,i})}. \quad (\text{A.7})$$

Here, p_{draw} refers to the uniform distributions from which the initial samples were drawn, and the numerators represent the target distributions associated with the population characterized by Φ . This weighting allows us to compute $\Omega_{\text{GW}}(f)$ while accounting for the desired population properties.

References

- Aasi, J. e. a. 2015, *Classical and Quantum Gravity*, 32, 074001
- Abbott, B. P., Abbott, R., Abbott, T. D., et al. 2020, *Living Reviews in Relativity*, 23
- Abbott, B. P., Abbott, R., Abbott, T. D., et al. 2017a, *Phys. Rev. Lett.*, 119, 161101
- Abbott, B. P. et al. 2017b, *Phys. Rev. Lett.*, 119, 141101
- Abbott, B. P. et al. 2021a, *Astrophys. J.*, 909, 218
- Abbott, R., Abbott, T. D., Abraham, S., et al. 2021b, *Phys. Rev. D*, 104, 022004
- Abbott, R., Abbott, T. D., Abraham, S., et al. 2021c, *The Astrophysical Journal Letters*, 913, L7
- Abbott, R., Abbott, T. D., Acernese, F., et al. 2017c, *Nature*, 551, 85–88
- Abbott, R., Abbott, T. D., Acernese, F., et al. 2023a, *The Astrophysical Journal*, 949, 76
- Abbott, R., Abbott, T. D., Acernese, F., et al. 2023b, *Phys. Rev. X*, 13, 041039
- Abbott, R., Abbott, T. D., Acernese, F., et al. 2021d, *Phys. Rev. D*, 104, 022004
- Abbott, R., Abbott, T. D., Acernese, F., et al. 2023c, *Phys. Rev. X*, 13, 011048
- Abbott, R. et al. 2023d, *Astrophys. J.*, 949, 76
- Acernese, F. e. a. 2014, *Classical and Quantum Gravity*, 32, 024001
- Ade, P. A. R., Aghanim, N., Arnaud, M., et al. 2016, *Astronomy & Astrophysics*, 594, A13
- Agarwal, A. et al. 2024 [arXiv:2412.14244]
- Ajith, P. et al. 2008, *Phys. Rev. D*, 77, 104017, [Erratum: *Phys. Rev. D* 79, 129901 (2009)]
- Allen, B. & Romano, J. D. 1999, *Physical Review D*, 59
- Aso, Y., Michimura, Y., Somiya, K., et al. 2013, *Physical Review D*, 88
- Bera, S., Rana, D., More, S., & Bose, S. 2020, *Astrophys. J.*, 902, 79
- Bom, C. R., Alfradique, V., Palmese, A., et al. 2024, *MNRAS*, 535, 961
- Borhanian, S. & Sathyaprakash, B. 2024, *Physical Review D*, 110

- Callister, T., Fishbach, M., Holz, D. E., & Farr, W. M. 2020, *The Astrophysical Journal Letters*, 896, L32
- Christensen, N. 1992, *Phys. Rev. D*, 46, 5250
- Cigarrán Díaz, C. & Mukherjee, S. 2022, *MNRAS*, 511, 2782
- Cousins, B., Schumacher, K., Chung, A. K.-W., et al. 2025, -
- Di Valentino, E., Mena, O., Pan, S., et al. 2021, *Classical and Quantum Gravity*, 38, 153001
- Ezquiaga, J. M. & Holz, D. E. 2021, *Astrophys. J. Lett.*, 909, L23
- Ezquiaga, J. M. & Holz, D. E. 2022, *Phys. Rev. Lett.*, 129, 061102
- Farr, W. M., Fishbach, M., Ye, J., & Holz, D. E. 2019, *ApJ*, 883, L42
- Ferri, J. a., Tashiro, I. L., Abramo, L. R., et al. 2024 [arXiv:2412.00202]
- Finke, A., Foffa, S., Iacovelli, F., Maggiore, M., & Mancarella, M. 2021, *Journal of Cosmology and Astroparticle Physics*, 2021, 026
- Fishbach, M., Farr, W. M., & Holz, D. E. 2020, *Astrophys. J. Lett.*, 891, L31
- Flanagan, E. E. 1993, *Phys. Rev. D*, 48, 2389
- Ghosh, T., More, S., Bera, S., & Bose, S. 2023 [arXiv:2312.16305]
- Gray, R., Beirnaert, F., Karathanasis, C., et al. 2023, *J. Cosmology Astropart. Phys.*, 2023, 023
- Gray, R., Hernandez, I. M., Qi, H., et al. 2020, *Phys. Rev. D*, 101, 122001
- Gray, R., Messenger, C., & Veitch, J. 2022, *Monthly Notices of the Royal Astronomical Society*, 512, 1127–1140
- Holz, D. E. & Hughes, S. A. 2005, *ApJ*, 629, 15
- Karathanasis, C., Mukherjee, S., & Mastrogiovanni, S. 2023, *Mon. Not. Roy. Astron. Soc.*, 523, 4539
- Libanore, S., Artale, M. C., Karagiannis, D., et al. 2021, *JCAP*, 02, 035
- Madau, P. & Dickinson, M. 2014, *Annual Review of Astronomy and Astrophysics*, 52, 415
- Mali, U. & Essick, R. 2024 [arXiv:2410.07416]
- Mancarella, M., Genoud-Prachex, E., & Maggiore, M. 2022, *Phys. Rev. D*, 105, 064030
- Mancarella, M., Iacovelli, F., Foffa, S., Muttoni, N., & Maggiore, M. 2024, *Phys. Rev. Lett.*, 133, 261001
- Mandel, I., Farr, W. M., & Gair, J. R. 2019, *Monthly Notices of the Royal Astronomical Society*, 486, 1086
- Mastrogiovanni, S., Laghi, D., Gray, R., et al. 2023, *Phys. Rev. D*, 108, 042002
- Mastrogiovanni, S., Laghi, D., Gray, R., et al. 2023a, *Phys. Rev. D*, 108, 042002
- Mastrogiovanni, S., Leyde, K., Karathanasis, C., et al. 2021, *Physical Review D*, 104, 104
- Mastrogiovanni, S., Leyde, K., Karathanasis, C., et al. 2021, *Phys. Rev. D*, 104, 062009
- Mastrogiovanni, S., Pierra, G., Perriès, S., et al. 2023b, ICAROGW: A python package for inference of astrophysical population properties of noisy, heterogeneous and incomplete observations
- Mukherjee, S. 2022, *Monthly Notices of the Royal Astronomical Society*, 515, 5495–5505
- Mukherjee, S., Krolewski, A., Wandelt, B. D., & Silk, J. 2024, *Astrophys. J.*, 975, 189
- Mukherjee, S., Wandelt, B. D., Nissanke, S. M., & Silvestri, A. 2021, *Phys. Rev. D*, 103, 043520
- Namikawa, T., Nishizawa, A., & Taruya, A. 2016a, *Phys. Rev. Lett.*, 116, 121302
- Namikawa, T., Nishizawa, A., & Taruya, A. 2016b, *Phys. Rev. D*, 94, 024013
- Ng, K. K. Y., Vitale, S., Farr, W. M., & Rodriguez, C. L. 2021, *The Astrophysical Journal Letters*, 913, L5
- Oguri, M. 2016, *Phys. Rev. D*, 93, 083511
- Palmese, A., Bom, C. R., Mucesh, S., & Hartley, W. G. 2023, *The Astrophysical Journal*, 943, 56
- Palmese, A., deVicente, J., Pereira, M. E. S., et al. 2020, *ApJ*, 900, L33
- Phinney, E. S. 2001, *A Practical Theorem on Gravitational Wave Backgrounds*
- Pierra, G., Mastrogiovanni, S., Perriès, S., & Mapelli, M. 2024, *Phys. Rev. D*, 109, 083504
- Renzini, A. I. et al. 2023, *Astrophys. J.*, 952, 25
- Romano, J. D. & Cornish, N. J. 2017, *Living Reviews in Relativity*, 20
- Scelfo, G., Boco, L., Lapi, A., & Viel, M. 2020, *JCAP*, 10, 045
- Schutz, B. F. 1986, *Nature*, 323, 310–311
- Soares-Santos, M., Palmese, A., et al. 2019, *ApJ*, 876, L7
- Talbot, C. & Thrane, E. 2018, *The Astrophysical Journal*, 856, 173
- Taylor, S. R., Gair, J. R., & Mandel, I. 2012, *Phys. Rev. D*, 85, 023535
- Turbang, K., Lalleman, M., Callister, T. A., & van Remortel, N. 2024, *The Astrophysical Journal*, 967, 142
- UNNIKRISHNAN, C. S. 2013, *International Journal of Modern Physics D*, 22, 1341010
- van Remortel, N., Janssens, K., & Turbang, K. 2023, *Progress in Particle and Nuclear Physics*, 128, 104003
- Vitale, S., Gerosa, D., Farr, W. M., & Taylor, S. R. 2021, *Inferring the Properties of a Population of Compact Binaries in Presence of Selection Effects* (Springer Singapore), 1–60
- Wei, J.-J. & Wu, X.-F. 2017, *The Astrophysical Journal*, 838, 160
- Yunes, N. & Siemens, X. 2013, *Living Reviews in Relativity*, 16
- Zazzera, S., Fonseca, J., Baker, T., & Clarkson, C. 2024 [arXiv:2412.01678]
- Zhang, P. 2018 [arXiv:1810.11915]